Landslide mapping from aerial photographs using change detection-based Markov random field

Zhongbin Li[a,b,*], Wenzhong Shi[a], Ping Lu[c], Lin Yan[b], Qunming Wang[d], Zelang Miao[a]

[a] *Department of Land Surveying and Geo-Informatics, The Hong Kong Polytechnic University, Hong Kong*
[b] *Geospatial Sciences Center of Excellence, South Dakota State University, Brookings, SD, USA*
[c] *College of Surveying and Geo-Informatics, Tongji University, Shanghai, China*
[d] *Lancaster Environment Center, Lancaster University, Lancaster, UK*

Abstract

Landslide mapping (LM) is essential for hazard prevention, mitigation, and vulnerability assessment. Despite the great efforts over the past few years, there is room for improvement in its accuracy and efficiency. Existing LM is primarily achieved using field surveys or visual interpretation of remote sensing images. However, such methods are highly labor-intensive and time-consuming, particularly over large areas. Thus, in this paper a change detection-based Markov random field (CDMRF) method is proposed for near-automatic LM from aerial orthophotos. The proposed CDMRF is applied to a landslide-prone site with an area of approximately 40 km^2 on Lantau Island, Hong Kong. Compared with the existing region-based level set evolution (RLSE), it has three main advantages: 1) it employs a more robust threshold method to generate the training samples; 2) it can identify landslides more accurately as it takes advantages of both the spectral and spatial contextual information of landslides; and 3) it needs little parameter tuning. Quantitative evaluation shows that it outperforms RLSE in the whole study area by almost 5.5% in *correctness* and by 4% in *quality*. To our knowledge, it is the first time CDMRF is used to LM from bitemporal aerial photographs. It is highly generic and has great potential for operational LM applications in large areas and also can be adapted for other sources of imagery data.

Keywords: Aerial photographs, change detection, landslide mapping (LM), Markov random field (MRF), region-based level set evolution (RLSE)

1. Introduction

Landslide hazards cause annual economic losses of nearly US$ 4 billion in Italy, over US$ 3 billion in Japan, more than US$ 1 billion in China (Klose et al., 2016), and at least US$ 2 billion in the United States (http://landslides.usgs.gov/). In Hong Kong, there are more than 100000 landslides on natural terrain, with almost 500 people killed in the past six decades (Choi and Cheung, 2013). The annual average expenditure over the last decade incurred by landslide prevention measures was about US$ 124 million (Choi and Cheung, 2013). Thus, landslide mapping (LM), including the date, spatial distribution, size, number, type, and morphological features of landslides, is essential for hazard prevention, mitigation, and

*Corresponding author
Email address: zhongbin.li@sdstate.edu (Zhongbin Li)

vulnerability assessment. In recent years, the progress of LM has been considerably facilitated by the development of remote sensing techniques (Metternicht et al., 2005; Ardizzone et al., 2007; Guzzetti et al., 2012; Tofani et al., 2013; Scaioni et al., 2014; Ciampalini et al., 2015). To date, numerous LM methods using optical remote sensing images have been developed and they are briefly reviewed in the following subsection.

1.1. Prior work

Prior LM methods can be roughly classified into five groups: visual interpretation-based, feature-based, change detection-based, topographic model-based, and machine learning-based methods. Related review articles can be referred to Guzzetti et al. (2012); Corominas et al. (2014). The studies of LM using synthetic aperture radar (SAR) data are not included in this section.

1.1.1. Visual interpretation-based methods

In Sato et al. (2007); Saba et al. (2010); Xu et al. (2015), earthquake-triggered landslides were visually interpreted from high resolution satellite images. Three different LM techniques using visual interpretation of aerial photos were compared in Galli et al. (2008). Similar comparisons can be found in Xu et al. (2014). Nearly 60000 landslide scarps were mapped from remote sensing images via visual interpretation in Gorum et al. (2011). In Ghosh et al. (2012), three types of landslides, i.e., shallow translational rockslides, shallow translational debris slides and deep-seated rockslides, were mapped by human interpretation of multitemporal remote sensing images. In Althuwaynee et al. (2015), a 12-year rainfall-induced landslide inventory map in the metropolitan area was visually delineated from aerial photos and SPOT-5 images. In Borrelli et al. (2014), rainfall-triggered landslides were mapped from aerial photos using visual interpretation which is aided by field surveys. In a different context Brunetti et al. (2014), landslides on Mars were visually interpreted from optical images. In Murillo-García et al. (2015), visual analysis of stereo pairs of GeoEye-1 images was applied to map rainfall-triggered landslides. A recent study found that visual interpretation of aerial photos is still the widely used LM method (Pellicani and Spilotro, 2015). In practice, however, visual interpretation is often labor-intensive and time-consuming.

1.1.2. Feature-based methods

Generally, the spectral, textural, morphological and topographic features are combined for LM. For example, landslides were mapped using the spectral, spatial contextual information and morphometric features in Martha et al. (2010); Lahousse et al. (2011); Aksoy and Ercanoglu (2012); Rau et al. (2014). In Lu et al. (2011); Martha et al. (2012), object-oriented change detection methods were developed for LM from multitemporal satellite images. In Martha et al. (2011), optimal segments generated by object-based image analysis (OBIA) and terrain curvature derived from DTM were combined for landslide detection and classification in mountainous areas. In van Den Eeckhaut et al. (2012), landslides in forested areas were identified by using multiple types of features derived from LiDAR data. Results in Moosavi et al. (2014) showed that OBIA outperforms pixel-based methods in LM from high resolution remote sensing images. In a recent study (Pradhan et al., 2015), landslides in a tropical urban area were detected using OBIA which combines airborne LiDAR data and Quickbird images.

1.1.3. Change detection-based methods

In some studies, landslides were mapped by differencing co-registered images or digital elevation models (DEMs) acquired over the same geographical position at different times. In van Westen and Getahun (2003), landslide evolution maps in Tessina, Italy were obtained via multitemporal aerial photographs interpretation and landslide volumetric changes were estimated by multitemporal DEMs analysis. In Hervás et al. (2003), landslides in the same area were mapped using bitemporal change detection of aerial photographs. In Tsutsui et al. (2007), multitemporal DEMs derived from SPOT-5 imagery were used to detect earthquake- and typhoon-triggered mountainous landslides and estimate their volumes. The similar application can be found in Pesci et al. (2011). In Yang and Chen (2010), LM was converted into the change analysis of the multitemporal normalized difference vegetation index (NDVI) from Landsat TM image and Advanced Spaceborne Thermal Emission and Reflection Radiometer image. In Mondini et al. (2011b,a), four different types of change detection techniques, i.e., dNDVI, spectral angle, principal component analysis, and independent component analysis, were combined to map shallow landslides from 8 m bitemporal satellite images. In Ventura et al. (2011), multitemporal LiDAR-derived digital terrain models (DTMs) were used to track the evolution of active rock landslides. More recently, change vector analysis (CVA) and level set method were integrated to map shallow debris flows from bitemporal aerial photos in Hong Kong (Li et al., 2016). Results indicated that region-based level set evolution (RLSE) outperforms edge-based LSE in LM.

1.1.4. Topographic model-based methods

In recent years, digital topographic models have been widely used for LM as they can provide detailed geomorphological features. In McKean and Roering (2004); Glenn et al. (2006); Trevisani et al. (2012); Tarolli et al. (2012); Razak et al. (2013); Giordan et al. (2013), DEM derived from LiDAR was used to analyze the landslide surface geomorphological features. In Bichler et al. (2004), DTM derived from remote sensing images was used to map 3D landslides on a plateau in Canada. LiDAR-derived DEMs were used to identify rainfall-induced landslides in a hilly area (Ardizzone et al., 2007) and forested landslides in a mountainous area (Chen et al., 2014). In Booth et al. (2009), LiDAR-derived DEM combining signal processing techniques was exploited to map deep-seated landslides. In Kurtz et al. (2014), landslide morphological features (e.g., slope and curvature) derived from DTM were utilized for mapping shallow and slow-moving landslides. The application of LiDAR-derived DEM for LM has been comprehensively reviewed in Jaboyedoff et al. (2012); Tarolli (2014).

1.1.5. Machine learning-based methods

In Borghuis et al. (2007), maximum likelihood classifier was used to map typhoon-triggered landslides in rugged area from 10 m SPOT-5 images. In Chang et al. (2007), a generalized positive Boolean function-based classifier was trained using spectral and morphological features for landslide classification. Probabilistic latent semantic analysis was applied to LM in semi-arid regions from GeoEye-1 images in Cheng et al. (2013). In Mondini et al. (2013), the inventory maps of rainfall-induced shallow landslides were produced using Bayesian inference. In Chen et al. (2014), random forest was trained using features derived from DTM to identify forested landslides. Support vector machine trained using backscatter and texture features was applied to detect slough slides along earthen levees in Mahrooghy et al. (2015).

The above brief review suggests that LM, despite the past efforts, remains a challenging task. There is significant demand for improvement in the accuracy and the degree of automation of LM (van Westen et al., 2006; Guzzetti et al., 2012). Although field surveys and visual interpretation of remote sensing images generally can provide reliable results, they are highly labor-intensive, time-consuming (Galli et al., 2008), and sometimes impractical. Thus, this paper attempts to propose a more accurate and automated LM method.

1.2. Our work

This paper is a further development of our previous work (Li et al., 2016), in which landslides were mapped from bitemporal aerial photos using LSE. Despite the decent performance of LSE, it has constraints regarding accuracy, automation and robustness considering large-area LM applications. In particular, LSE only utilizes the spectral information of landslides, which is sometimes not adequate to obtain reliable results. In addition, there are many free parameters in LSE that need to be tuned in practical applications, and however, it is not easy to obtain the optimal parameter values. Therefore, in this paper we propose a new change detection-based Markov random field (CDMRF) for near-automatic LM. Compared with the existing LM methods, CDMRF has the following attractive characteristics: 1) it takes into account both the spectral and spatial contextual information of landslides; 2) it has a great level of automation; and 3) it requires little parameter tuning.

2. Study area and dataset

The study area, with a total land area of approximately 40 km^2, is located on western Lantau Island, Hong Kong (Fig. 1). It is characterized by steep terrain, 40% of which is steeper than 25°. The highest point in the study area is Ling Wui Shan with a height of 490 m. There are mainly two land cover types: subtropical vegetation (grasslands, shrublands, and woodlands) and developed infrastructures (human settlements, roads, temples, and reservoirs). More detailed vegetation information can be retrieved at Hong Kong Herbarium (http://herbarium.gov.hk/). Most peaks are grassy and lower slopes are often covered with shrubs and forests. The study area is underlain primarily by Upper Jurassic silicic volcanic tuffs and lavas (Sewell et al., 2015). Most peaks in the study area are formed by the highly weathered tuffs and lavas, which produce loose materials. Although the internal friction and cohesion of the materials on steep slopes resist gravitational collapse, the infiltration of rain fills spaces between loose soil and rock, which potentially leads to unstable slopes (Owen and Shaw, 2007). The main landslide type in the study area is debris flow, which is a combination of soil, rock, organic matter, air, and water that flows under gravity.

The average annual precipitation in this area is nearly 2400 mm due to the humid subtropical climate. On 7 June 2008, Lantau Island was affected by an extreme rainstorm in an unprecedented manner. The total rainfall reached 307 mm within 24 h. More than 2400 landslides were triggered and they were mainly shallow debris flows involving highly mobile top-soil, bouldery colluvium, and weathered rock. Most of them traveled long distances, posing great threats to life and property. For LM in the study area, the pre- and post-event

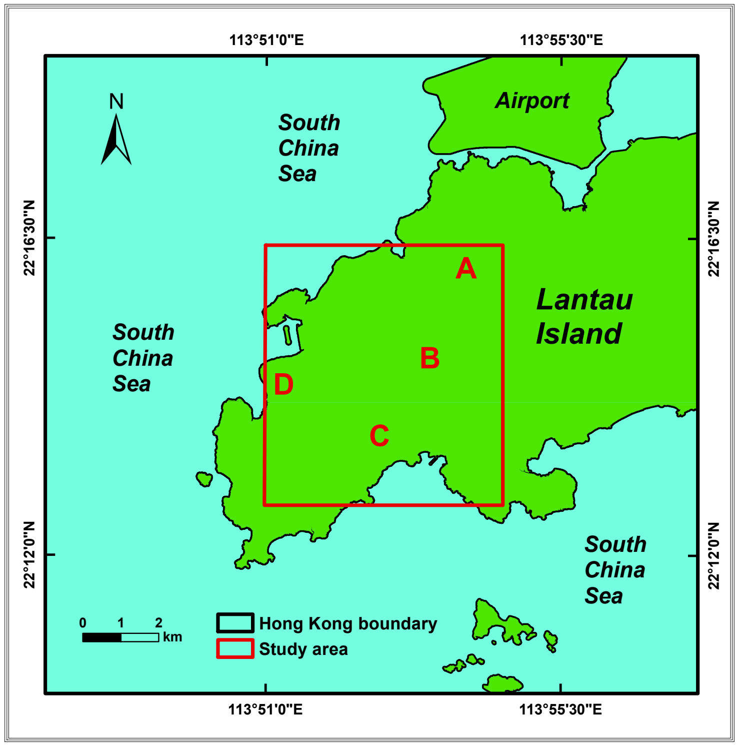

Fig. 1. Study area with sub-areas A to D highlighted on Lantau Island, Hong Kong.

RGB aerial photos [Fig. 2(a) and (b)] with a spatial resolution of 0.5 m and a size of 11843 × 13397 pixels (about 40 km^2) are used. They were acquired by Zeiss RMK TOP 15 Aerial Survey Camera System at a flying height of approximately 2400 m in December 2005 and on November 20, 2008, respectively. As can be seen in Fig. 2(b), there are numerous landslides with different sizes, shapes, and spatial distributions. Most of them occurred in shrublands and grasslands. They are often spectrally heterogeneous due to the mixed materials such as weathered volcanic tuffs, soils, and grasses. Thus, in some areas the landslide boundaries are blurry, which often pose great challenges to edge-based methods (Li et al., 2016). In addition, there are numerous spectrally similar volcanic tuffs and lavas surrounding landslides in some areas, which also complicate LM substantially.

The proposed CDMRF in this paper will be applied to LM in the study area and four sub-areas A to D (Fig. 1) will be examined in detail. For accuracy evaluation, the results will be compared with the manually digitized reference map truth which is shown in Fig. 2(d).

3. Methodology

The proposed CDMRF is composed of the following four principal steps (Fig. 3). First, the pre-processing including geometric correction, radiometric correction, and masking is applied to the original bitemporal aerial photos. Then, the difference image (DI) is automatically generated using change vector analysis (CVA). Next, the training samples of landslides and non-landslides are generated from the post-event aerial orthophoto using a multi-threshold method. Finally, LM is achieved using MRF.

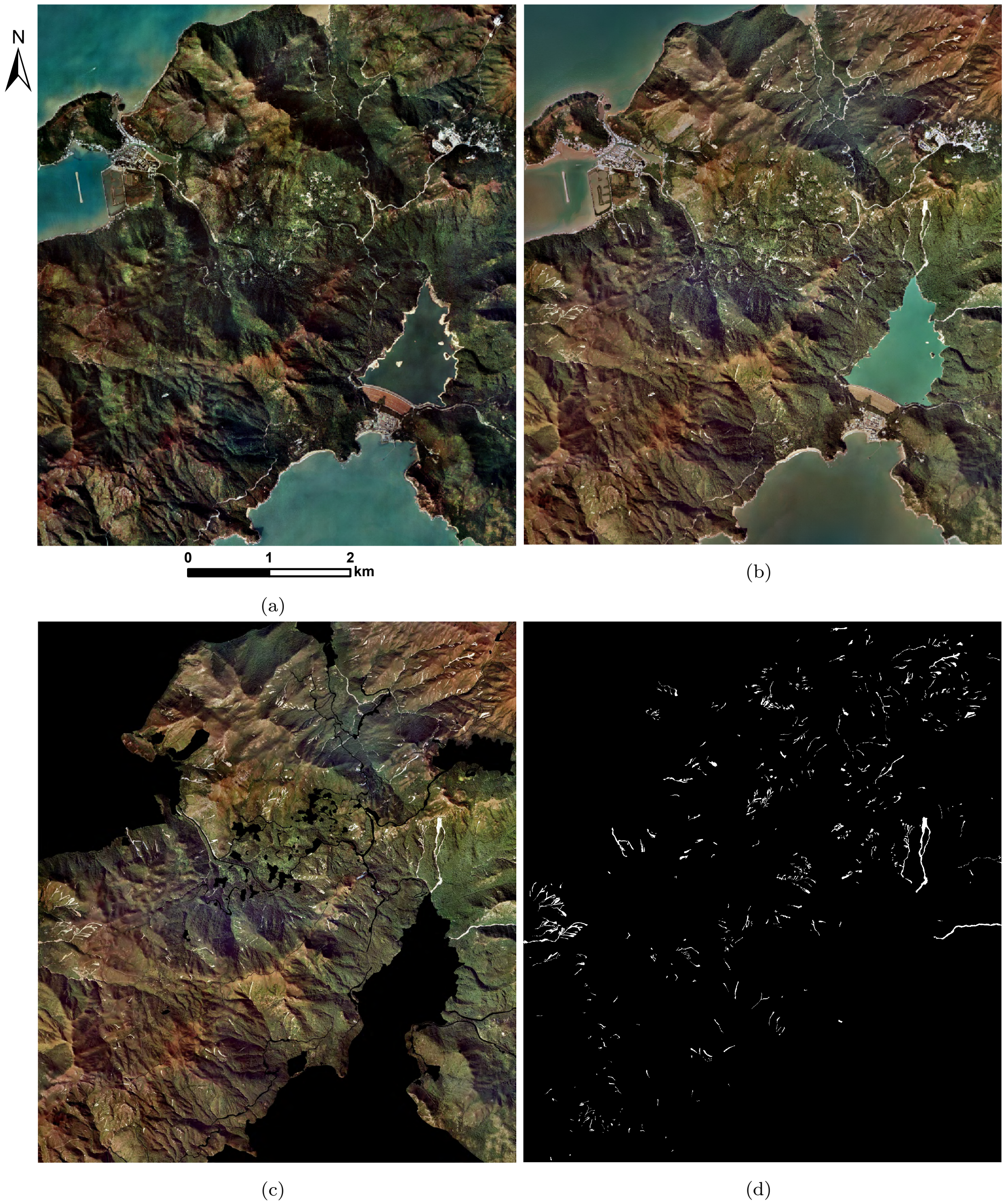

Fig. 2. Datasets. (a) and (b) Pre- and post-event aerial orthophotos. (c) Masked post-event orthophoto. (d) Reference map.

3.1. Pre-processing

The pre-processing includes geometric correction, radiometric correction, and masking. A more detailed description can be found in Li et al. (2016). For geometric correction, photo distortions and topographic relief were rectified. The relief displacement was removed using Hong Kong DTM, which was also used for ortho-rectification. For radiometric correction, absolute radiometric correction was not applied to the bitemporal aerial orthophotos because there is no *in situ* atmospheric data available at the time of sensor overpasses. For bitemporal change analysis, relative radiometric correction is generally used to make bitemporal images

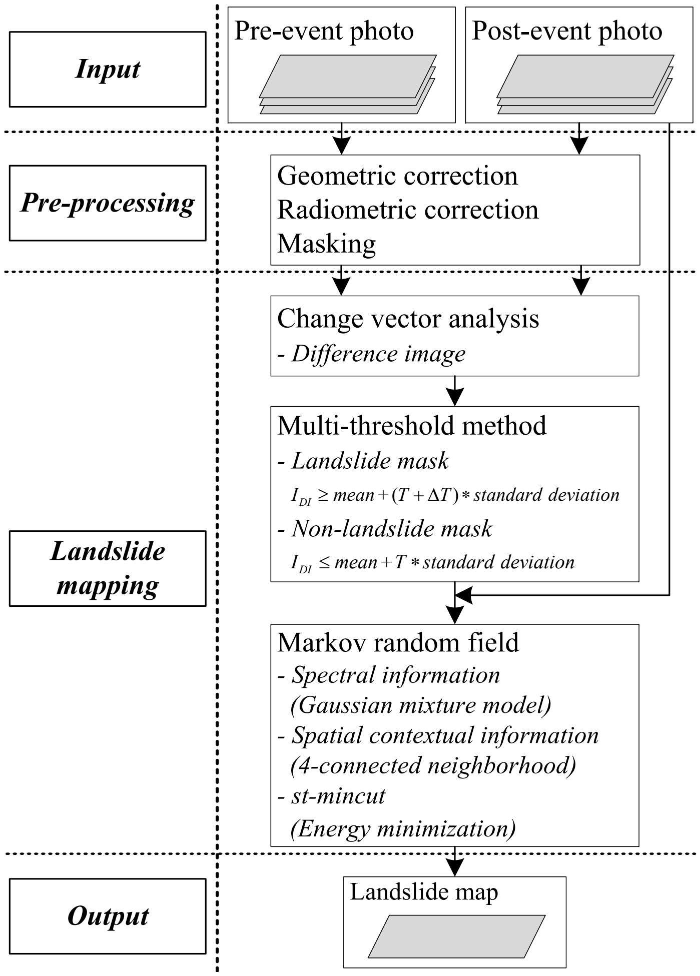

Fig. 3. Flowchart of the proposed landslide mapping method.

appear as if they are acquired under similar atmospheric and illumination conditions. However, it may lead to inaccurate change analysis in real applications as it often substantially reduces the magnitude of spectral differences, which has been identified in Yang and Lo (2002). Thus, radiometric adjustment and color balancing were applied to the bitemporal orthophotos. The former can effectively compensate for visual effects such as hot spots, lens vignetting, and color variations. The latter can adjust adjacent aerial photos to match in color and brightness. Finally, the seamless and color-balanced orthophoto mosaic with a scale of 1:5000 was produced. In addition, the developed infrastructures (e.g., human settlements, roads, temples, and reservoirs) often cause errors in multitemporal change analysis. To eliminate the potential errors, they were masked in post-event aerial orthophoto using digital topographic maps which were provided by Lands Department, Hong Kong [Fig. 2(c)].

3.2. The generation of difference image

Like the work in Li et al. (2016), DI is automatically generated using CVA (Lambin and Strahler, 1994). CVA is defined as follows:

$$\rho(I) = \left[\sum_{b=1}^{n} (I_{t_1} - I_{t_2})_b^2 \right]^{1/2} \tag{1}$$

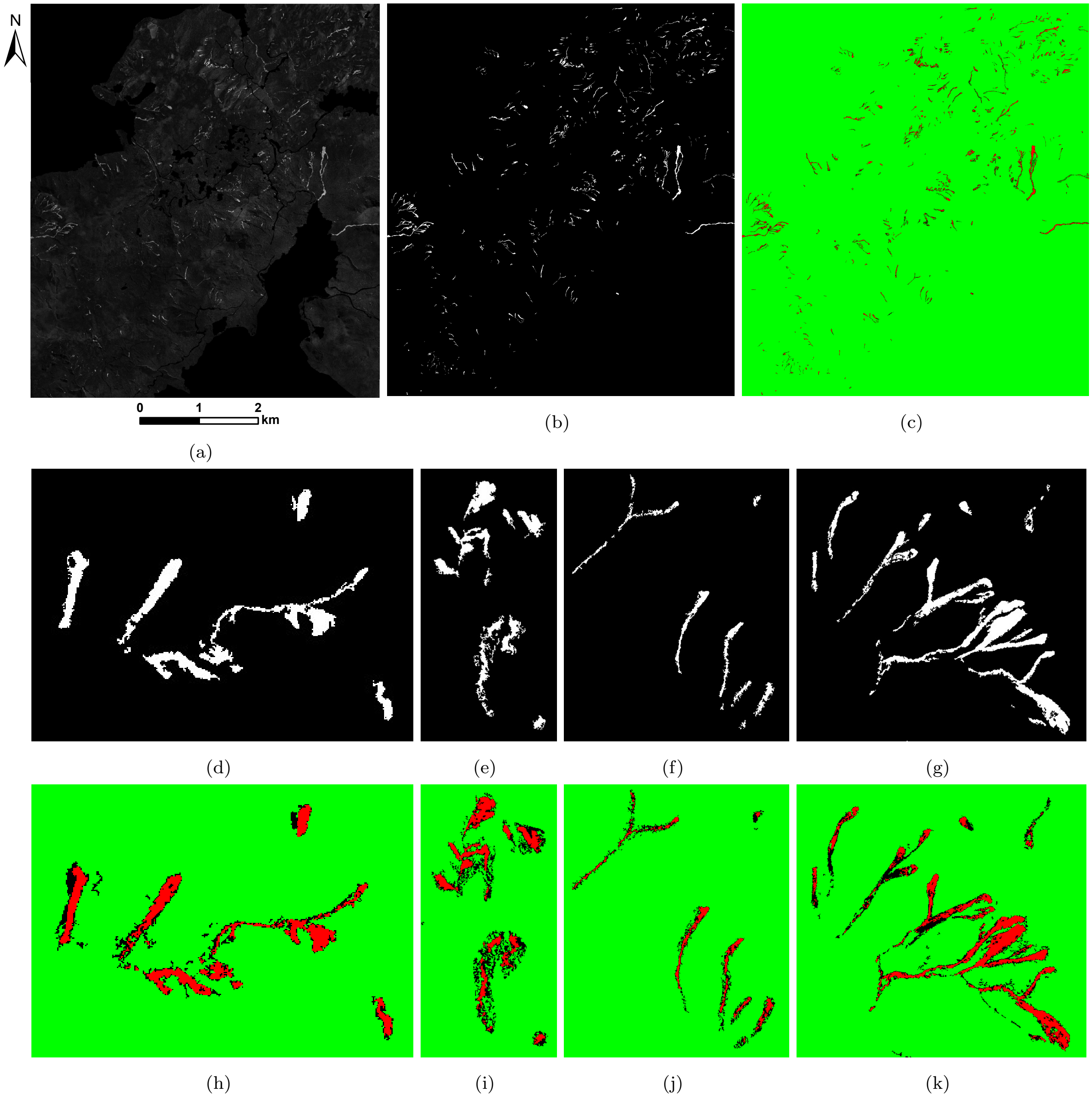

Fig. 4. Difference image (DI), the initial zero-level set (ZLS), and training sample masks. (a) DI generated by CVA. (b) The initial ZLS (white for landslides and black for non-landslides) generated by the single threshold method in Li et al. (2016) with $\alpha = 1.5$. (c) Training sample masks (red, green, and black for landslides, non-landslides, and uncertain areas) generated by the multi-threshold method in Eq. (2) with $T = 1$ and $\Delta T = 1.5$. (d) - (g) Initial ZLSs in sub-areas A to D. (h) - (k) Training sample masks in sub-areas A to D.

in which I_{t_1} and I_{t_2} are pixel values of the pixel I at the times t_1 and t_2, b is the band number, $\rho(I)$ is the magnitude of the change vector of the pixel I. The pixels with greater values of $\rho(I)$ in DI generally correspond to candidate landslides, as shown in Fig. 4(a). However, they are often not homogeneous as landslides are generally spectrally heterogeneous. In addition, there are often other errors in DI caused by phenology variations or illumination differences. Thus, using DI alone cannot discriminate landslides from non-landslides accurately. To address this challenge, LM is achieved using MRF in this paper. Traditionally, MRF is an interactive object segmentation method which requires human interaction to provide the training samples. However, human interaction is highly labor-intensive in real applications. To reduce the load on users, the training samples of landslides and non-landslides in this paper are generated from the post-event aerial orthophoto using an effective multi-threshold method.

3.3. The generation of training samples

Generally, the brightest and darkest pixels in DI represent landslides and non-landslides, respectively. Thus, the training sample masks of landslides and non-landslides can be generated by the following multi-threshold method (Chuvieco et al., 2002):

$$I_{DI} = \begin{cases} landslide, & \text{if } \rho(I) \geq \mu + (T + \Delta T) * \sigma_{DI} \\ uncertain\ area, & \text{if } \mu + (T + \Delta T) * \sigma_{DI} > \rho(I) > \mu + T * \sigma_{DI} \\ non - landslide, & \text{if } \rho(I) \leq \mu + T * \sigma_{DI} \end{cases} \tag{2}$$

where $I_{DI} = \rho(I)$ is the intensity value of the pixel I in DI, $T \in \mathbb{Z}^+$ and $\Delta T \in \mathbb{R}^+$ are parameters, μ is the mean of DI, and σ_{DI} is the standard deviation of DI. In Eq. (2), the pixels in DI with intensity values less than or equal to $(\mu + T * \sigma_{DI})$ are classed as non-landslides; whereas the pixels with intensity values greater than or equal to $[\mu + (T + \Delta T) * \sigma_{DI}]$ are regarded as landslides; and those falling into this interval are considered to be uncertain areas.

According to the multi-threshold method Eq. (2), the training sample masks for the whole study area can be generated. As illustrated in Fig. 4(c), red, green, and black areas represent landslides, non-landslides, and uncertain areas, respectively. The training sample masks for the four sub-areas A to D are presented in Fig. 4(h) to (k). The final training samples are obtained by superimposing the training sample masks onto the post-event aerial orthophoto and collecting the corresponding RGB values of the landslide and non-landslide pixels. Then, the next step is to map landslides using MRF.

3.4. Markov random field

Once the training samples are determined, landslides can be mapped using MRF (Fig. 5). MRF can assign each pixel in the uncertain areas a label (1 for landslides or 0 for non-landslides), which forms a label set that minimizes the following energy function (Szeliski et al., 2008):

$$\begin{gathered} E(L) = E_u(L) + \lambda \cdot E_p(L) \\ \hat{L} = \operatorname{argmin}_L E(L) \end{gathered} \tag{3}$$

where $E_u(L)$ and $E_p(L)$ are the unary potential and pairwise potential, respectively. They are balanced by a weighting coefficient λ. $L = (l_1, l_2, ..., l_n)$ is a label set, $l_i \in \{0, 1\}$ is the label of the ith pixel I_i, and n is the pixel number in DI. $\hat{L}$ is the minimum of the energy function $E(L)$.

3.4.1. The unary potential

The unary potential $E_u(L)$ can ensure that the label set L is consistent with the training samples, and it is defined as

$$E_u(L) = \sum_{i \in C_1} V_i(l_i) \tag{4}$$

where C_1 is the single-site clique. $V_i(l_i)$ is often defined as follows

$$V_i(l_i) = \begin{cases} -\log\left(p(O|I_i)\right), & \text{if } l_i = 1 \\ -\log\left(p(B|I_i)\right), & \text{if } l_i = 0 \end{cases} \tag{5}$$

in which $p(O|I_i)$ is the posterior probability of the uncertain pixel I_i belonging to the object O (i.e., landslide). The similar annotation $p(B|I_i)$ is used for the background B (i.e., non-landslide). $V_i(l_i)$ is often modeled as two Gaussian mixture models (GMMs) (Rother et al., 2004): one for landslide and the other for non-landslide (Fig. 5).

A GMM is generally defined as a weighted linear combination of M Gaussian components:

$$p\left(\mathbf{x}|\Theta\right) = \sum_{i=1}^{M} \omega_i g\left(\mathbf{x}|\boldsymbol{\mu}_i, \boldsymbol{\Sigma}_i\right) \tag{6}$$

where $\mathbf{x} \in \mathbb{R}^d$ is the data vector (i.e., RGB values), ω_i are scalar weights and $\sum_{i=1}^{M} \omega_i = 1$, and $g\left(\mathbf{x}|\boldsymbol{\mu}_i, \boldsymbol{\Sigma}_i\right)$ is the ith Gaussian component:

$$g\left(\mathbf{x}|\boldsymbol{\mu}_i, \boldsymbol{\Sigma}_i\right) = \frac{1}{\sqrt{(2\pi)^d \det \boldsymbol{\Sigma}_i}} \exp\left[-\frac{1}{2}(\mathbf{x}-\boldsymbol{\mu}_i)^{\intercal} {\boldsymbol{\Sigma}_i}^{-1}(\mathbf{x}-\boldsymbol{\mu}_i)\right] \tag{7}$$

in which $\boldsymbol{\mu}_i$ and $\boldsymbol{\Sigma}_i$ are the mean and covariance, and $\Theta = \{\omega_i, \boldsymbol{\mu}_i, \boldsymbol{\Sigma}_i\}, i = 1, ..., M$ is the set of parameters.

Two GMMs need to be trained from the training samples: one for landslide (i.e., GMM_1) and the other for non-landslide (i.e., GMM_2), as presented in Fig. 5. In each GMM, 5 Gaussian components are used and each component represents a spectral (color) class. Too many components may lead to overfitting. In this paper, the parameters of the two GMMs (i.e., ω_i, $\boldsymbol{\mu}_i$ and $\boldsymbol{\Sigma}_i$) are separately estimated using a hierarchical clustering algorithm called TSVQ (Gersho and Gray, 2012). Its efficiency has been identified in Carlotto (2005) and its principle is briefly described as follows.

The basic idea behind TSVQ is that the original training samples (either landslide or non-landslide) are viewed as a single cluster, which is further grouped into M clusters (here $M = 5$) and each cluster corresponds to a Gaussian component. More specifically, the mean and covariance matrices of the original cluster are first computed (Li et al., 2014). Then, the eigenvalue and eigenvector of the covariance matrix can be obtained. The eigenvector corresponding to the greatest eigenvalue points in the direction of the greatest cluster variation. The initial cluster is then split into two parts by a vector that is perpendicular to that eigenvector while passing through the mean. Next, the new mean and covariance matrices of the sub-clusters are computed. The splitting repeats $M - 1$ times until M Gaussian components are obtained. In each final component, the pixels are assigned with the same label and counted. Thus, the mean $\boldsymbol{\mu}_i$ and covariance $\boldsymbol{\Sigma}_i$ of the ith component can be readily obtained, and their weights ω_i are in proportion to their pixel numbers. In this way, GMM_1 and GMM_2 can be determined.

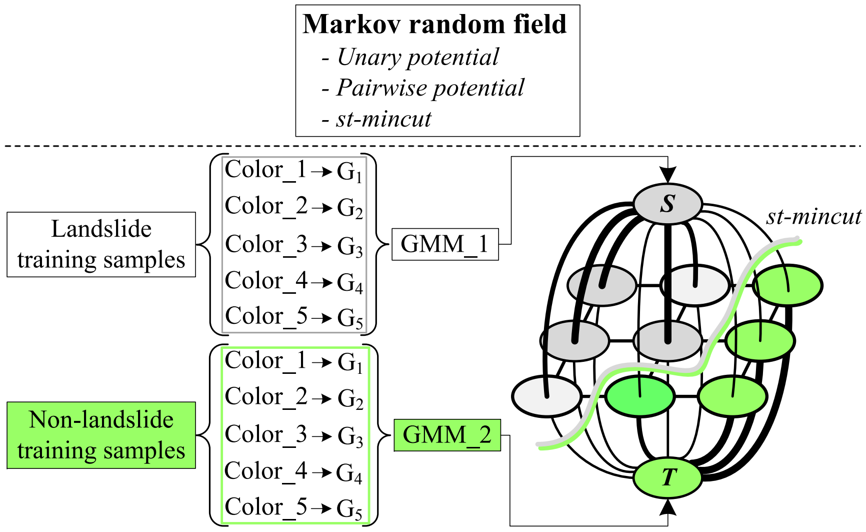

Fig. 5. Diagram of MRF. Color_i is the ith Gaussian component G_i, $i = 1, ..., n$. n is fixed at 5 in this paper. Each GMM consists of 5 Gaussian components. GMM_1 and GMM_2 are the likelihood of landslide and non-landslide pixels, respectively. They are used to calculate the unary potential in Eq. (3). Gray and green nodes represent the landslide and non-landslide pixels, respectively. S and T correspond to the GMM_1 and GMM_2. The edge weights measure the degree of similarity of neighboring pixels (4-neighborhood system). They are employed to calculate the pairwise potential in Eq. (3). The larger the weights, the thicker the edges. The separations of the weak edges will automatically partition landslides from non-landslides.

Once GMMs are obtained, the posterior probabilities of the uncertain pixels can be computed by using Bayes' theorem:

$$p(O|I_i) = \frac{p(I_i|O)p(O)}{p(I_i|O)p(O) + p(I_i|B)p(B)} \tag{8}$$

where $p(O|I_i)$ is the posterior probability that the uncertain pixel I_i belongs to the class of landslide O. $p(I_i|O)$ is the likelihood of the landslide pixel. Here, $p(I_i|O) = \text{GMM\_1}$. Analogous notations are used for the class of non-landslide B, and there are $p(B|I_i) = 1 - p(O|I_i)$ and $p(I_i|B) = \text{GMM\_2}$. $p(O)$ and $p(B)$ are prior probabilities of the landslide and non-landslide, respectively, and $p(O) = p(B) = \frac{1}{2}$.

3.4.2. The pairwise potential

The pairwise potential $E_p(L)$ takes account of the similarity of neighboring pixels, which makes it able to ensure the spatial smoothness of the final labels. It is defined as

$$E_p(L) = \sum_{(i,j) \in C_2} V_{ij}(l_i, l_j) \tag{9}$$

in which C_2 is the pair-site clique(i.e., 4-connected neighborhood). $V_{ij}(l_i, l_j) = \exp\left(-\beta(I_i - I_j)^2\right) \cdot \delta(l_i, l_j)$, in which the term $(I_i - I_j)^2$ is used to capture the spatial contextual information of landslides or non-landslides by measuring the spectral differences among the 4-neighborhood pixels. When the spectral difference between the two neighboring pixels is very small, they will be assigned with the same labels; otherwise, they will be assigned with different labels. $\beta = \left(2\langle(I_i - I_j)^2\rangle\right)^{-1}$, where $\langle\cdot\rangle$ is the expectation operator over the entire image. β acts as a contrast adjuster. When the image contrast is low (i.e., the value of $(I_i - I_j)$ is small), it becomes great; otherwise, it becomes small. $\delta(l_i, l_j)$ is defined as follows:

$$\delta(l_i, l_j) = \begin{cases} 0, & \text{if } l_i = l_j \\ 1, & \text{if } l_i \neq l_j \end{cases} \tag{10}$$

3.4.3. Energy minimization

The minimization of the energy function Eq. (3) is implemented via the *st*-mincut algorithm (Boykov and Kolmogorov, 2004). Specifically, the pixels and their 4-neighborhood links are regarded as vertices V and edges E in a graph $G = \langle V, E \rangle$. Generally, two additional vertices called source S and sink T are used as label sets, i.e., 1 for landslide and 0 for non-landslide. They correspond to the GMM_1 and GMM_2, respectively (Fig. 5). Each edge between the neighboring pixels has a weight that measures the degree of similarity. All the pixels also connect with S and T. The edge weights are defined by the probabilities that the pixels belong to the landslide or non-landslide. The greater the weights are, the stronger the edges become, as shown in Fig. 5.

In a graph $G = \langle V, E \rangle$, a cut is defined as a partition that separate the vertices V into two disjoint sets V_O and $V_B = V \setminus V_O$. For LM, it corresponds to the weak edges that connect landslide vertices V_O and non-landslide vertices V_B. The partitions of these edges will lead to the automatic separation of the landslide from the non-landslide. These weak edges are called mincut due to the minimal sum of weights, as shown in Fig. 5. Thus, LM is essentially equivalent to finding the mincut. In computer vision, mincut has been a well studied energy minimization algorithm. In this paper, the implementation of the mincut employs the algorithm proposed in Boykov and Kolmogorov (2004). For more details, please visit the helpful websites at http://vision.csd.uwo.ca/code/ and http://vision.middlebury.edu/MRF/.

The program in this paper is run under MATLAB R2013a 64 b in Windows 7 OS with a Lenovo workstation of Intel(R) Core(TM) i7-3770 CPU @ 3.40 GHz, 16 GB RAM. The source code is available upon request.

4. Experimental results

4.1. Experimental setup

To verify the advantages of the proposed CDMRF in LM, it is compared with RLSE used in Li et al. (2016) recently. For visual evaluation, both CDMRF and RLSE are applied to the whole study area where four sub-areas are examined in detail (Fig. 1). For quantitative evaluation, the results of CDMRF and RLSE are compared with the manually digitized reference maps. Three quantitative evaluation indices are used: $Completeness = P_{lm}/P_r$, $Correctness = P_{lm}/P_l$, and $Quality = P_{lm}/(P_l + P_{rum})$, where P_{lm} is the total pixel number of the identified landslides that are matched with the reference maps, P_r is the total pixel number of the reference maps, P_l is the total pixel number of the identified landslides, and P_{rum} is the total pixel number of the reference maps that are unmatched with the identified landslides.

The parameter values used for CDMRF are as follows: $T = 1.0$, $\Delta T = 1.5$, and $\lambda = 50$. The values of T and ΔT are determined via trial and error. The parameter values used for RLSE in this paper are as

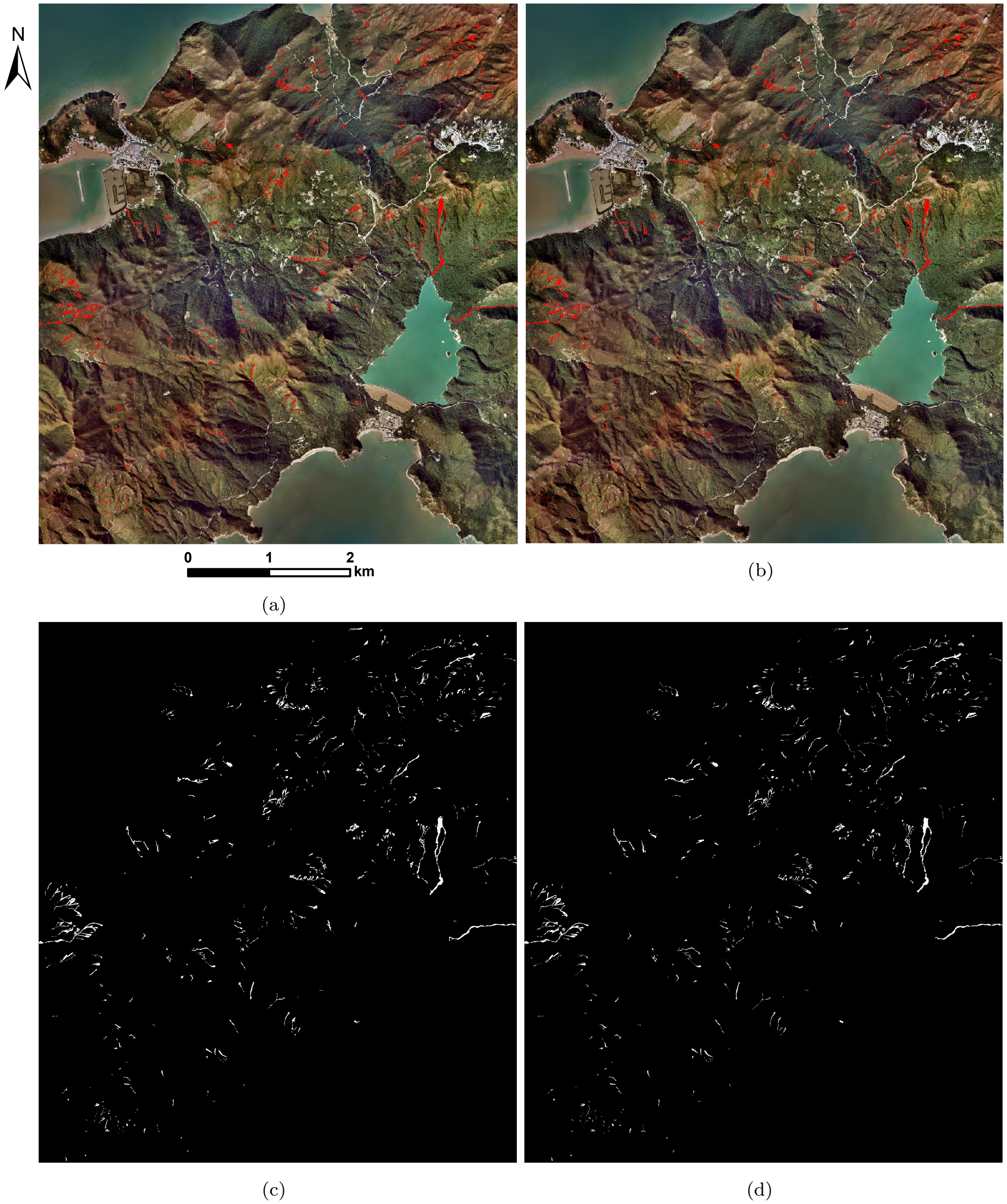

Fig. 6. LM results of RLSE and the proposed CDMRF in the whole study area. (a) and (b) Results of RLSE and CDMRF overlaid on the post-event aerial orthophoto, respectively. (c) and (d) The corresponding binary results of RLSE and CDMRF.

follows: $\alpha = 1.5$, $c_0 = 1.0$, the standard deviation of the Gaussian filter σ is fixed at 1.0, the template size of the Gaussian filter is 9×9, and time step $\Delta t = 5.0$. The use of a relatively small value of Δt for RLSE is to relieve over-detection or boundary leakage.

4.2. Visual evaluation

4.2.1. The whole study area

The pre- and post-event aerial orthophotos for the whole study area are shown in Fig. 2(a) and (b). The reference map is presented in Fig. 2(d). The LM results of RLSE and CDMRF are shown in Fig. 6(a) and (b), respectively. The corresponding binary results are presented in Fig. 6(c) and (d).

As shown in Fig. 6(a) and (c), RLSE can identify the elongated landslides well due to the use of the regional statistics. However, it often results in over-detection and incomplete detection of some landslides. The primary causes are threefold. First, although Gaussian filter used in the numerical implementation of RLSE can smooth the ZLCs, it often leads to inaccurate boundary detection (Perona and Malik, 1990) or even boundary leakage. Second, the initial ZLCs generated using the single-threshold method for the whole study area in Li et al. (2016) are not accurate in some local areas. As can be seen in Fig. 4(b) and (d) to (g), some of them fall into the nearby non-landslide areas. In practice, it is difficult to obtain an appropriate threshold that can accurately discriminate landslides from non-landslides over large areas. Third, although RLSE takes advantage of regional intensity means, it is essentially a two-phase segmentation method, namely, it can only handle bright or dark objects at a time. Thus, it sometimes cannot identify the spectral heterogeneous landslides completely.

In contrast, the proposed CDMRF performs much better. As shown in Fig. 6(b) and (d), CDMRF can effectively identify blurry, elongated, and even spectrally heterogeneous landslides. To sum up, it has the following two appealing advantages over RLSE: 1) to generate more reliable training samples [see Fig. 4(c) and (h) to (k)], it exploits a more robust multi-threshold method rather than the vulnerable single thresholding used in RLSE; 2) in addition to the spectral information, it also takes into account the spatial contextual information of landslides to determine the uncertain areas. Thus, it takes full advantage of the similarity of the neighboring pixels, which makes it able to map landslides more completely and accurately. For further detailed comparisons between RLSE and CDMRF, their LM results in four sub-areas covered with different land use types are further examined in the following subsections.

4.2.2. Sub-area A

The LM results of RLSE and CDMRF in sub-area A are presented in Fig. 7. The pre- and post-event aerial orthophotos are shown in Fig. 7(a) and (b). As can be seen, this sub-area is covered with dense grasslands and there are phenological variations between the two photos. The reference map is given in Fig. 7(c). Fig. 7(d) to (f) show the RLSE results, while Fig. 7(g) to (i) present the CDMRF results. Two sub-areas indicated by red and green arrows in Fig. 7(d) are examined in detail. As can be seen, the red-arrow indicated area is erroneously identified as the landslide by RLSE due to the inaccurate initial ZLC generated by the single threshold method in Li et al. (2016) [Fig. 4(d)]. Although the initial ZLC is accurate in the green-arrow indicated area, RLSE cannot detect the elongated and spectrally heterogeneous landslide completely. This is mainly because RLSE is essentially a two-phase object segmentation method, which makes it only effective to extract either the brighter objects or the darker objects at a time. However, with the similar training samples [see Fig. 4(h)], CDMRF can achieve better performance. Using both the

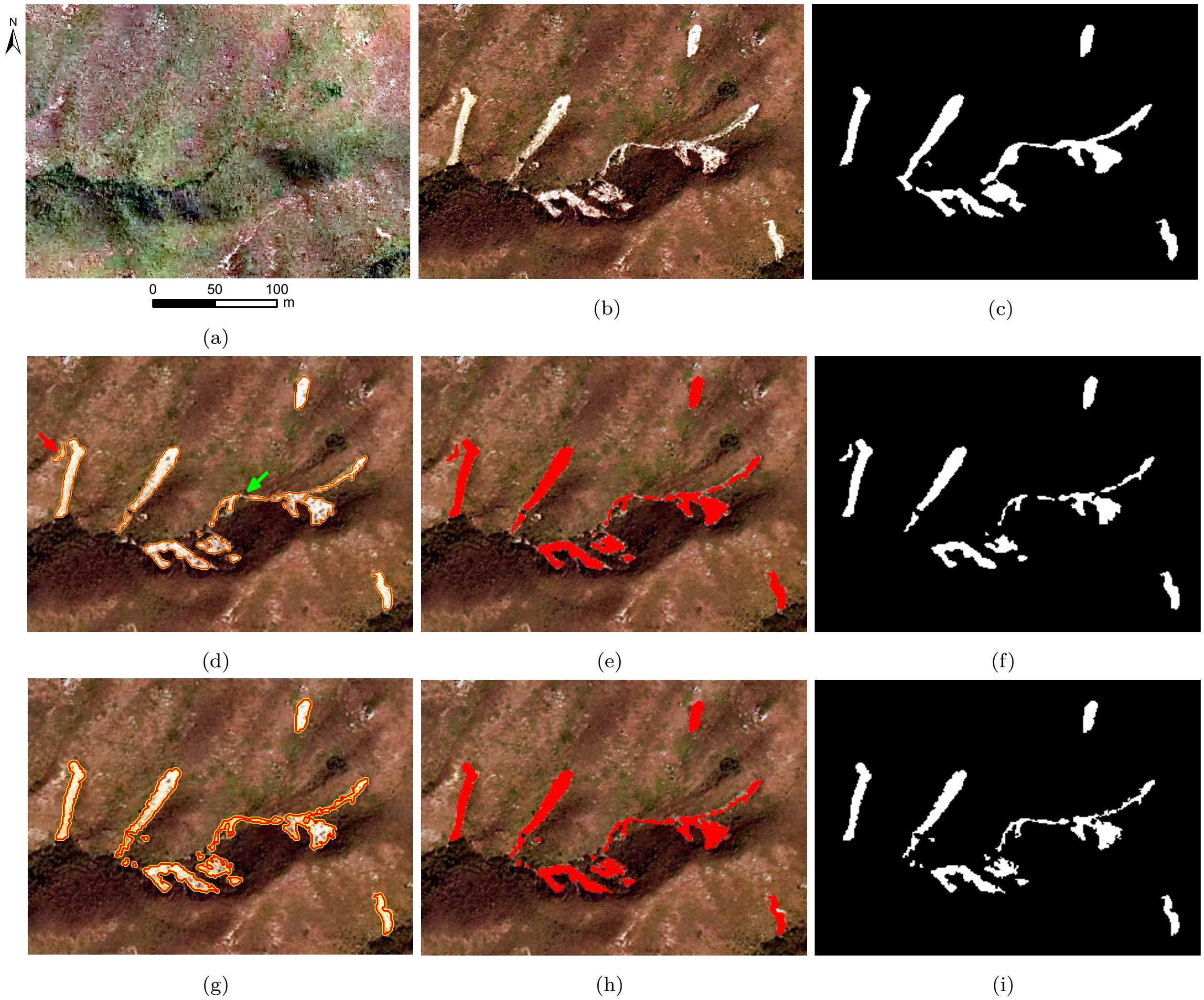

Fig. 7. LM results in sub-area A. (a) and (b) Pre- and post-event aerial orthophotos. (c) reference map. (d)-(f) Results of RLSE: zero-level curve (ZLC) in (d), ZLS in (e), and the binary results in (f). (g)-(i) Result of CDMRF: landslide boundaries in (g), landslides in (h), and the binary results in (i). See main text for detailed explanations of the arrows in (d).

spectral and spatial contextual information of landslides, it is able to estimate the red-arrow indicated area as the non-landslide accurately while identifying the elongated landslide more completely than RLSE.

4.2.3. Sub-area B

The LM results in sub-area B are shown in Fig. 8. The pre- and post-event orthophotos are presented in Fig. 8(a) and (b). The reference map is shown in Fig. 8(c). This area is covered with dense grasslands on upper slopes and dense woodlands on lower slopes. Landslides in this area are spectrally relatively homogeneous. The results of RLSE are shown in Fig. 8(d) to (f). As can be seen in areas indicated by the green arrow in Fig. 8(d), the ZLCs of RLSE pass through blurry landslide boundaries and the non-landslides are erroneously identified as landslides, leading to serious over-detection. The main reason is that the initial ZLCs in these areas are not accurate enough. As can be seen in Fig. 4(e), most of them fall into the non-landslide areas due to the inaccurate threshold generated by the single threshold method in Li et al. (2016).

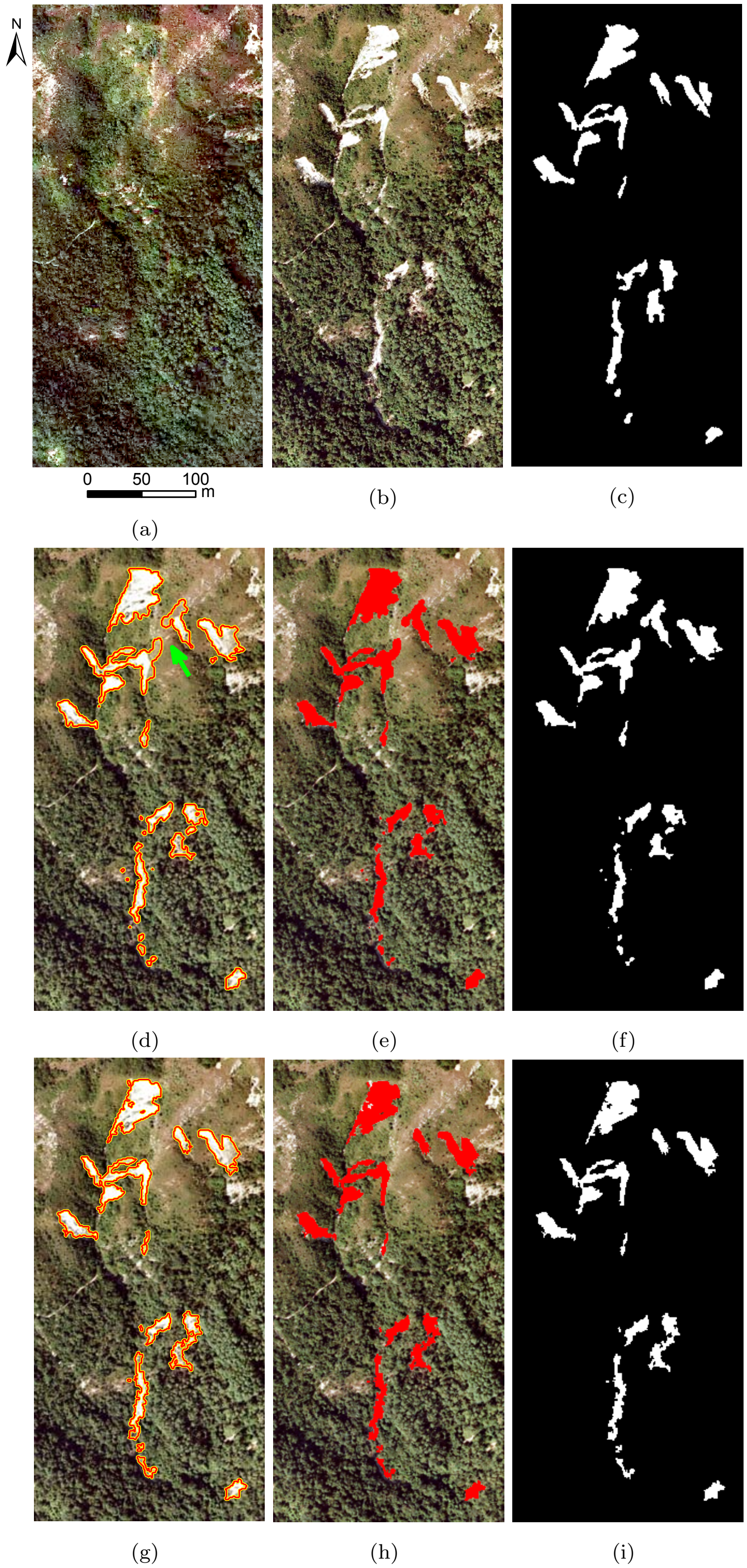

Fig. 8. LM results in sub-area B. (a) and (b) Pre- and post-event aerial orthophotos. (c) reference map. (d)-(f) Results of RLSE: ZLC in (d), ZLS in (e), and the binary results in (f). (g)-(i) Result of CDMRF: landslide boundaries in (g), landslides in (h), and the binary results in (i). See main text for detailed explanations of the arrow in (d).

In contrast, CDMRF performs much better than RLSE in this example. As presented in Fig. 8(g) to (i), it is able to identify the landslide boundaries accurately. Due to the use of the spatial contextual information of landslides, it can effectively avoid the over-detection of landslide boundaries.

4.2.4. Sub-area C

Fig. 9 shows the LM results of sub-area C. The pre- and post-event orthophotos are presented in Fig. 9(a) and (b). The reference map is shown in Fig. 9(c). This area is partly covered with sparse grasslands and partly with shrublands. There are some outcrops of volcanic tuffs and lavas surrounding the landslides. Due to the similar spectral signatures, they are identified as landslides by RLSE, as indicated by the green arrows in Fig. 9(d). Thus, they result in the over-detection of landslides in the result of RLSE. However, CDMRF can identify landslides accurately. The multi-threshold method can effectively eliminate the spectrally similar surroundings. Thus, there is no over-detection arising in the results of CDMRF, as shown in Fig. 9(g) to (i). In addition, almost all the landslides in this area are elongated. Some of them are shaded by shrubs, which make them spectrally heterogeneous and discontinuous. Both RLSE and CDMRF cannot handle the shadowed landslides well and thus they cannot obtain the complete landslides in this example.

4.2.5. Sub-area D

Fig. 10 presents the LM results of sub-area D. The pre- and post-event orthophotos are shown in Fig. 10(a) and (b). The reference map is shown in Fig. 10(c). As can be seen, this area is mainly covered with dense grasslands on upper slopes and sparse woodlands on lower slopes. Most landslides in this area are mixed with grasses and thus they are spectrally heterogeneous, especially the elongated landslide branches indicated by red arrows in Fig. 10(d). Both RLSE and CDMRF cannot detect them well, thus leading to incomplete detection of landslides. Overall, however, they can obtain favorable results in this example. Compared with RLSE, CDMRF clearly performs better in the following two sub-areas. First, RLSE can only extract small part of the spectrally heterogeneous landslide indicated by the cyan arrow in Fig. 10(d). However, CDMRF can identify this landslide more completely, as presented in Fig. 10(g) to (i). Second, there is incomplete detection of landslide in the results of RLSE. As indicated by the green arrow in Fig. 10(d), RLSE cannot detect the small and spectral heterogeneous landslide branch completely. However, CDMRF can identify it effectively.

4.3. Quantitative evaluation

For quantitative evaluation, the LM results of RLSE and the proposed CDMRF are compared with the manually digitized reference maps [Fig. 2(d)] using the previously mentioned indices, i.e., *Completeness*, *Correctness*, and *Quality*. The numerical results are presented in Table 1 and the corresponding bar chart is illustrated in Fig. 11.

As shown in Fig. 11(a), CDMRF can extract more complete landslides than RLSE in sub-areas A and B. That is mainly due to the fact that it takes advantage of both the spectral and contextual information of landslides. In contrast to CDMRF, RLSE has better performance in the whole study area, sub-areas C and D. RLSE can effectively extract the elongated landslides using regional intensity means. The single threshold

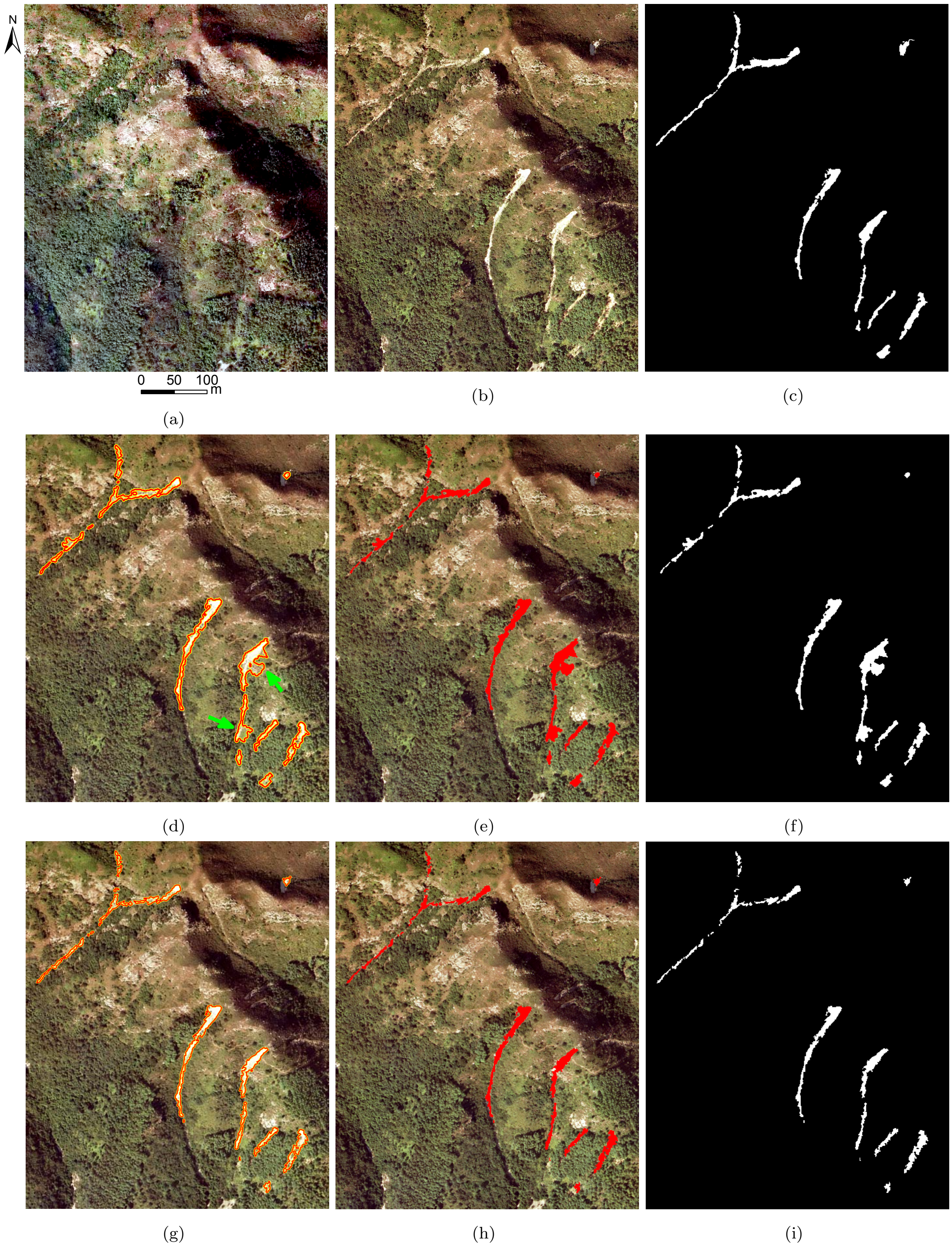

Fig. 9. LM results in sub-area C. (a) and (b) Pre- and post-event aerial orthophotos. (c) reference map. (d)-(f) Results of RLSE: ZLC in (d), ZLS in (e), and the binary results in (f). (g)-(i) Result of CDMRF: landslide boundaries in (g), landslides in (h), and the binary results in (i). See main text for detailed explanations of the arrows in (d).

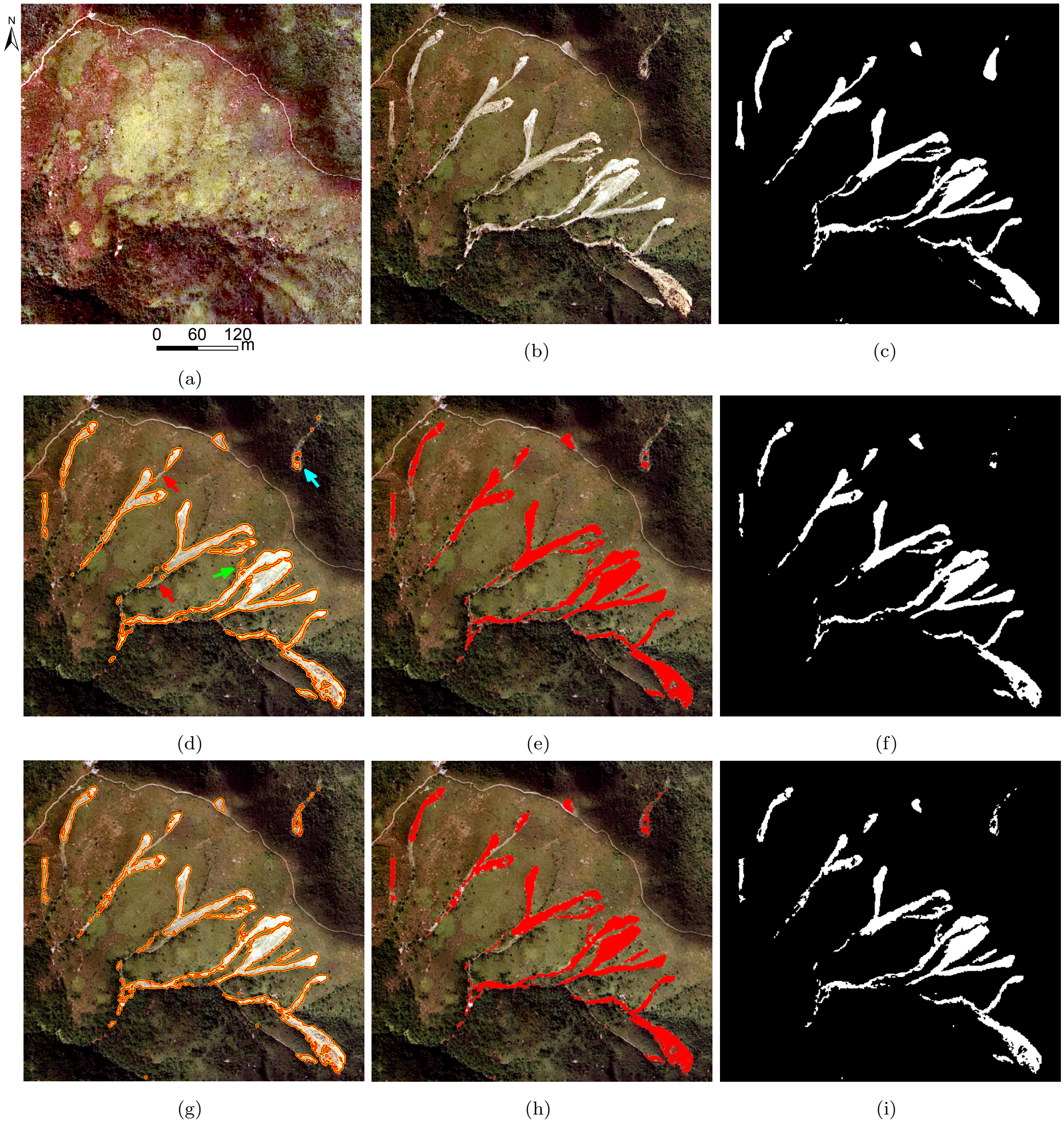

Fig. 10. LM results in sub-area D. (a) and (b) Pre- and post-event aerial orthophotos. (c) reference map. (d)-(f) Results of RLSE: ZLC in (d), ZLS in (e), and the binary results in (f). (g)-(i) Result of CDMRF: landslide boundaries in (g), landslides in (h), and the binary results in (i). See main text for detailed explanations of the arrows in (d).

method used in RLSE often leads to the over-detection of landslides, which, however, makes RLSE able to extract more complete landslides.

From the perspective of correctness, CDMRF overwhelmingly excels RLSE in all the experiments, as can be seen in Fig. 11(b). In the whole study area, CDMRF outperforms RLSE by almost 5.5%, as can be seen in Table 1. The Gaussian filter enables RLSE to obtain smooth landslide boundaries. However, it sometimes results in over-detection of landslides, thus degrading the correctness of RLSE. Compared with RLSE, CDMRF performs better, especially in the sub-areas B and C. It takes full advantage of the similarity

Table 1.

Quantitative evaluation of LM. Red values indicate the better performance

Study areas	Methods	Evaluation indices (%)		
		Completeness	*Correctness*	*Quality*
The whole	RLSE	75.4	88.5	63.1
	CDMRF	73.6	**93.8**	**67.1**
Sub-area A	RLSE	75.5	95.9	70.9
	CDMRF	**78.7**	**96.7**	**74.7**
Sub-area B	RLSE	85.4	76.5	56.0
	CDMRF	**85.6**	**86.6**	**67.6**
Sub-area C	RLSE	81.2	74.7	52.4
	CDMRF	70.9	**89.3**	**60.6**
Sub-area D	RLSE	80.7	95.7	75.3
	CDMRF	79.7	**96.9**	**75.8**

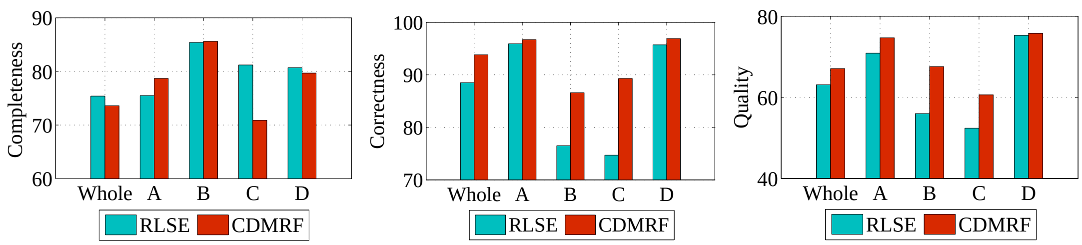

(a) (b) (c)

Fig. 11. Quantitative evaluation of the proposed CDMRF for LM in the whole study area and four sub-areas A to D. (a). Completeness. (b) Correctness. (c) Quality.

of neighboring pixels and thus landslides can be identified more accurately.

In terms of the overall quality, CDMRF clearly outperforms RLSE in all the experiments, as shown in Fig. 11(c). In particular, CDMRF surpasses RLSE in the whole study area by 4%, as shown in Table 1. The main reason for the decent performance is that it takes into account both the spectral and spatial contextual information of landslides. Due to the over-detection or boundary leakage, the qualities of RLSE in sub-areas B and C are less than 60%.

To sum up, the quantitative evaluation clearly shows that CDMRF has competitive advantages over RLSE.

5. Discussion

5.1. The advantages of the proposed method

The effectiveness of the proposed CDMRF has been verified visually and quantitatively. Compared with the existing RLSE, it has the following appealing advantages.

1. It is a near-automatic LM method. It combines change detection technique and MRF effectively. It exploits change vector analysis (CVA) and a multi-threshold method to generate the training samples of landslides and non-landslides for MRF. Thus, it can reduce the load on users substantially.

2. In addition to the spectral information, it also takes into account the spatial contextual information of landslides, which makes it capable of detecting landslides more accurately.
3. It requires little parameter tuning. As previously mentioned, there are 5 and 3 free parameters that need to be tuned in RLSE and CDMRF, respectively. Thus, this would make it more operational in real applications.
4. Although it is just applied to LM from bitemporal aerial photos on Lantau Island, Hong Kong, it is actually a generic land cover change detection method. It can be definitely used to other types of remote sensing images (e.g., high-resolution multispectral images) and other study areas.

5.2. Parameter analysis

Compared with RLSE, the proposed CDMRF only has three parameters, as mentioned before. Thus, it needs much less parameter tuning. The first one is T in Eq. (2). It determines the lower threshold that is used to generate the training samples of non-landslides. Its value is generally related to the brightness of DI. The brighter the DI, the greater its value. In this paper, it is fixed at 1.0 for the whole study area via trial and error. The second parameter is ΔT in Eq. (2). Together with T, it determines the upper threshold that is used to generate the training samples of landslides. In the meantime, it determines the range of the interval between the upper and lower thresholds. The pixels in DI with intensity values falling in this interval are classed as uncertain pixels, which are finally determined using MRF. Thus, ΔT can impact the quality of LM. In this paper, it is fixed at 1.5 for the whole study area via trial and error. The third parameter is λ in Eq. (3). It balances the unary potential and pairwise potential. It is fixed at 50 throughout the experiments according to the recommendations in Rother et al. (2004); Szeliski et al. (2008).

5.3. Future work

The proposed CDMRF consists of two main steps: change detection-based training samples generation and MRF-based LM. It is generic to be applied to other types of remote sensing data. For instance, it can be readily used to the pansharpened and co-registered bitemporal WorldView-3 satellite imagery which has 30 cm spatial resolution and 8 multispectral bands for LM with higher spatial resolution. Also, for the capabilities of the SAR sensors to penetrate clouds, the applications of CDMRF to SAR data for real-time or near real-time LM will be investigated.

CDMRF was tested to map rainfall-triggered shallow landslides in this paper. For deep-seated or translational landslides, they can be mapped by CDMRF as long as the spectral differences between landslides and the surroundings are distinct enough in the used aerial images. However, if the differences are too subtle to be reflected in aerial images, they cannot be effectively detected; in this case, the remotely-sensed imageries with higher spatial or temporal resolutions are needed. CDMRF also has difficulty in detecting the covered landslides such as those located under forest, which are not visible in optical images, and this requires the usage of the sensors that can penetrate tree crowns, such as LiDAR (Eeckhaut et al., 2007; Razak et al., 2011; van Den Eeckhaut et al., 2012; Chen et al., 2014).

3D LM would be more useful and popular in real applications. This paper only focused on 2D LM from aerial photos. DTM or other related features are not taken into account in the proposed CDMRF. Thus, the future work can be directed at 3D LM using DTM.

In recent years, extreme rainstorms are becoming increasingly frequent due to the global climate change. A recent study has pointed out that landslide activity in Hong Kong may increase due to the global warming (Sewell et al., 2015). Thus, it would be interesting to extend the research from LM to exploring the relationship between landslide activity and local climate (Wood et al., 2015), especially the extreme rainstorm.

6. Conclusion

A new and near-automatic landslide mapping (LM) method, termed as change detection-based Markov random field (CDMRF), has been presented in this paper. First, the difference image (DI) was automatically generated from pre- and post-event aerial orthophotos using change vector analysis (CVA). Then, the training samples of landslide and non-landslides were generated from the post-event aerial orthophoto using a multi-threshold method. Finally, LM was achieved using MRF.

The proposed CDMRF has been applied to a landslide site with an area of approximately 40 km^2 on Lantau Island, Hong Kong. The LM results have been compared with the reference maps and those of RLSE visually and quantitatively. Quantitative evaluation has shown that it outperforms RLSE in the whole study area by almost 5.5% in *correctness* and by 4% in *quality*. Experiments have demonstrated its appealing characteristics: 1) it can achieve LM in a near-automatic manner; 2) it takes into account both the spectral and spatial contextual information of landslides, thus obtaining more accurate results; 3) it requires little parameter tuning; and 4) it is highly generic and has strong potential to be adapted for other remote sensing data sources and other landslide-prone sites. Given its efficiency and accuracy, it could be applied to rapid responses and emergency managements of natural hazards.

Acknowledgment

This work was supported in part by The Hong Kong Polytechnic University projects (nos. 1-ZE24, 1-ZVE8, and 1-ZEA5) and the National Natural Science Foundation of China (no. 41201424). We would like to thank Geotechnical Engineer Mr. Shum from Civil Engineering and Development Department, Hong Kong and Chief Photogrammetrist Mr. Heung from Lands Department, Hong Kong for providing us with aerial orthophotos and valuable suggestions on ortho-rectification and radiometric correction of aerial photos. We also would like to thank the handling editor and the two anonymous reviewers for their detailed and insightful comments, which substantially enhanced the presentation of the paper.

References

Aksoy, B., Ercanoglu, M., 2012. Landslide identification and classification by object-based image analysis and fuzzy logic: An example from the Azdavay region (Kastamonu, Turkey). Computer and Geosciences 38 (1), 87–98.

Althuwaynee, O. F., Pradhan, B., Ahmad, N., 2015. Estimation of rainfall threshold and its use in landslide hazard mapping of Kuala Lumpur metropolitan and surrounding areas. Landslides 12 (5), 861–875.

Ardizzone, F., Cardinali, M., Galli, M., Guzzetti, F., Reichenbach, P., 2007. Identification and mapping of recent rainfall-induced landslides using elevation data collected by airborne Lidar. Natural Hazards and Earth System Sciences 7 (6), 637–650.

Bichler, A., Bobrowsky, P., Best, M., Douma, M., Hunter, J., Calvert, T., Burns, R., 2004. Three-dimensional mapping of a landslide using a multi-geophysical approach: the Quesnel Forks landslide. Landslides 1 (1), 29–40.

Booth, A. M., Roering, J. J., Perron, J. T., 2009. Automated landslide mapping using spectral analysis and high-resolution topographic data: Puget Sound lowlands, Washington, and Portland Hills, Oregon. Geomorphology 109 (3), 132–147.

Borghuis, A., Chang, K., Lee, H., 2007. Comparison between automated and manual mapping of typhoon-triggered landslides from SPOT-5 imagery. International Journal of Remote Sensing 28 (8), 1843–1856.

Borrelli, L., Antronico, L., Gullà, G., Sorriso-Valvo, G. M., 2014. Geology, geomorphology and dynamics of the 15 February 2010 Maierato landslide (Calabria, Italy). Geomorphology 208, 50–73.

Boykov, Y., Kolmogorov, V., 2004. An experimental comparison of min-cut/max-flow algorithms for energy minimization in vision. IEEE Transactions on Pattern Analysis and Machine Intelligence 26 (9), 1124–1137.

Brunetti, M. T., Guzzetti, F., Cardinali, M., Fiorucci, F., Santangelo, M., Mancinelli, P., Komatsu, G., Borselli, L., 2014. Analysis of a new geomorphological inventory of landslides in Valles Marineris, Mars. Earth and Planetary Science Letters 405, 156–168.

Carlotto, M. J., 2005. A cluster-based approach for detecting man-made objects and changes in imagery. IEEE Transactions on Geoscience and Remote Sensing 43 (2), 374–387.

Chang, Y.-L., Liang, L.-S., Han, C.-C., Fang, J.-P., Liang, W.-Y., Chen, K.-S., 2007. Multisource data fusion for landslide classification using generalized positive Boolean functions. IEEE Transactions on Geoscience and Remote Sensing 45 (6), 1697–1708.

Chen, W., Li, X., Wang, Y., Chen, G., Liu, S., 2014. Forested landslide detection using LiDAR data and the random forest algorithm: A case study of the Three Gorges, China. Remote Sensing of Environment 152, 291–301.

Cheng, G., Guo, L., Zhao, T., Han, J., Li, H., Fang, J., 2013. Automatic landslide detection from remote-sensing imagery using a scene classification method based on BoVW and pLSA. International Journal of Remote Sensing 34 (1), 45–59.

Choi, K., Cheung, R. W., 2013. Landslide disaster prevention and mitigation through works in Hong Kong. Journal of Rock Mechanics and Geotechnical Engineering 5 (5), 354–365.

Chuvieco, E., Martin, M. P., Palacios, A., 2002. Assessment of different spectral indices in the red-near-infrared spectral domain for burned land discrimination. International Journal of Remote Sensing 23 (23), 5103–5110.

Ciampalini, A., Raspini, F., Bianchini, S., Frodella, W., Bardi, F., Lagomarsino, D., Di Traglia, F., Moretti, S., Proietti, C., Pagliara, P., Onori, R., Corazza, A., Duro, A., Basile, G., Casagli, N., 2015. Remote sensing as tool for development of landslide databases: The case of the Messina Province (Italy) geodatabase. Geomorphology 249, 103–118.

Corominas, J., van Westen, C., Frattini, P., Cascini, L., Malet, J.-P., Fotopoulou, S., Catani, F., van Den Eeckhaut, M., Mavrouli, O., Agliardi, F., Pitilakis, K., Winter, M., Pastor, M., Ferlisi, S., Tofani, V., Hervás, J., Smith, J., 2014. Recommendations for the quantitative analysis of landslide risk. Bulletin of Engineering Geology and the Environment 73 (2), 209–263.

Eeckhaut, M., Poesen, J., Verstraeten, G., Vanacker, V., Nyssen, J., Moeyersons, J., van Beek, L., Vandekerckhove, L., 2007. Use of LIDAR-derived images for mapping old landslides under forest. Earth Surface Processes and Landforms 32 (5), 754–769.

Galli, M., Ardizzone, F., Cardinali, M., Guzzetti, F., Reichenbach, P., 2008. Comparing landslide inventory maps. Geomorphology 94 (3), 268–289.

Gersho, A., Gray, R. M., 2012. Vector quantization and signal compression. Vol. 159. Springer Science & Business Media.

Ghosh, S., van Westen, C. J., Carranza, E. J. M., Jetten, V. G., Cardinali, M., Rossi, M., Guzzetti, F., 2012. Generating event-based landslide maps in a data-scarce Himalayan environment for estimating temporal and magnitude probabilities. Engineering Geology 128, 49–62.

Giordan, D., Allasia, P., Manconi, A., Baldo, M., Santangelo, M., Cardinali, M., Corazza, A., Albanese, V., Lollino, G., Guzzetti, F., 2013. Morphological and kinematic evolution of a large earthflow: The Montaguto landslide, southern Italy. Geomorphology 187, 61–79.

Glenn, N. F., Streutker, D. R., Chadwick, D. J., Thackray, G. D., Dorsch, S. J., 2006. Analysis of LiDAR-derived topographic information for characterizing and differentiating landslide morphology and activity. Geomorphology 73 (1), 131–148.

Gorum, T., Fan, X., van Westen, C. J., Huang, R. Q., Xu, Q., Tang, C., Wang, G., 2011. Distribution pattern of earthquake-induced landslides triggered by the 12 May 2008 Wenchuan earthquake. Geomorphology 133 (3), 152–167.

Guzzetti, F., Mondini, A. C., Cardinali, M., Fiorucci, F., Santangelo, M., Chang, K.-T., 2012. Landslide inventory maps: New tools for an old problem. Earth-Science Reviews 112 (1), 42–66.

Hervás, J., Barredo, J. I., Rosin, P. L., Pasuto, A., Mantovani, F., Silvano, S., 2003. Monitoring landslides from optical remotely sensed imagery: the case history of Tessina landslide, Italy. Geomorphology 54 (1), 63–75.

Jaboyedoff, M., Oppikofer, T., Abellán, A., Derron, M.-H., Loye, A., Metzger, R., Pedrazzini, A., 2012. Use of LIDAR in landslide investigations: a review. Natural Hazards 61 (1), 5–28.

Klose, M., Maurischat, P., Damm, B., 2016. Landslide impacts in Germany: A historical and socioeconomic perspective. Landslides 13 (1), 183–199.

Kurtz, C., Stumpf, A., Malet, J.-P., Gançarski, P., Puissant, A., Passat, N., 2014. Hierarchical extraction of landslides from multiresolution remotely sensed optical images. ISPRS Journal of Photogrammetry and Remote Sensing 87, 122–136.

Lahousse, T., Chang, K., Lin, Y., 2011. Landslide mapping with multi-scale object-based image analysis–a case study in the Baichi watershed, Taiwan. Natural Hazards and Earth System Sciences 11 (10), 2715–2726.

Lambin, E. F., Strahler, A. H., 1994. Indicators of land-cover change for change-vector analysis in multitemporal space at coarse spatial scales. International Journal of Remote Sensing 15 (10), 2099–2119.

Li, Z., Liu, Z., Shi, W., 2014. Semiautomatic airport runway extraction using a line-finder-aided level set evolution. IEEE Journal of Selected Topics in Applied Earth Observations and Remote Sensing 7 (12), 4738–4749.

Li, Z., Shi, W., Myint, S. W., Lu, P., Wang, Q., 2016. Semi-automated landslide inventory mapping from bitemporal aerial photographs using change detection and level set method. Remote Sensing of Environment 175, 215 – 230.

Lu, P., Stumpf, A., Kerle, N., Casagli, N., 2011. Object-oriented change detection for landslide rapid mapping. IEEE Geoscience and Remote Sensing Letters 8 (4), 701–705.

Mahrooghy, M., Aanstoos, J. V., Nobrega, R., Hasan, K., Prasad, S., Younan, N. H., et al., 2015. A machine learning framework for detecting landslides on earthen levees using spaceborne SAR imagery. IEEE Journal of Selected Topics in Applied Earth Observations and Remote Sensing, 3791 – 3801.

Martha, T. R., Kerle, N., Jetten, V., van Westen, C. J., Kumar, K. V., 2010. Characterising spectral, spatial and morphometric properties of landslides for semi-automatic detection using object-oriented methods. Geomorphology 116 (1), 24–36.

Martha, T. R., Kerle, N., van Westen, C. J., Jetten, V., Kumar, K. V., 2011. Segment optimization and data-driven thresholding for knowledge-based landslide detection by object-based image analysis. IEEE Transactions on Geoscience and Remote Sensing 49 (12), 4928–4943.

Martha, T. R., Kerle, N., van Westen, C. J., Jetten, V., Kumar, K. V., 2012. Object-oriented analysis of multi-temporal panchromatic images for creation of historical landslide inventories. ISPRS Journal of Photogrammetry and Remote Sensing 67, 105–119.

McKean, J., Roering, J., 2004. Objective landslide detection and surface morphology mapping using high-resolution airborne laser altimetry. Geomorphology 57 (3), 331–351.

Metternicht, G., Hurni, L., Gogu, R., 2005. Remote sensing of landslides: An analysis of the potential contribution to geo-spatial systems for hazard assessment in mountainous environments. Remote Sensing of Environment 98 (2), 284–303.

Mondini, A., Guzzetti, F., Reichenbach, P., Rossi, M., Cardinali, M., Ardizzone, F., 2011a. Semi-automatic recognition and mapping of rainfall induced shallow landslides using optical satellite images. Remote Sensing of Environment 115 (7), 1743–1757.

Mondini, A. C., Chang, K.-T., Yin, H.-Y., 2011b. Combining multiple change detection indices for mapping landslides triggered by typhoons. Geomorphology 134 (3), 440–451.

Mondini, A. C., Marchesini, I., Rossi, M., Chang, K.-T., Pasquariello, G., Guzzetti, F., 2013. Bayesian framework for mapping and classifying shallow landslides exploiting remote sensing and topographic data. Geomorphology 201, 135–147.

Moosavi, V., Talebi, A., Shirmohammadi, B., 2014. Producing a landslide inventory map using pixel-based and object-oriented approaches optimized by Taguchi method. Geomorphology 204, 646–656.

Murillo-García, F. G., Alcántara-Ayala, I., Ardizzone, F., Cardinali, M., Fiourucci, F., Guzzetti, F., 2015. Satellite stereoscopic pair images of very high resolution: a step forward for the development of landslide inventories. Landslides 12 (2), 277–291.

Owen, B., Shaw, R., 2007. Hong Kong landscapes: shaping the barren rock. Hong Kong University Press.

Pellicani, R., Spilotro, G., 2015. Evaluating the quality of landslide inventory maps: comparison between archive and surveyed inventories for the Daunia region (Apulia, Southern Italy). Bulletin of Engineering Geology and the Environment 74 (2), 357–367.

Perona, P., Malik, J., 1990. Scale-space and edge detection using anisotropic diffusion. IEEE Transactions on Pattern Analysis and Machine Intelligence 12 (7), 629–639.

Pesci, A., Teza, G., Casula, G., Loddo, F., De Martino, P., Dolce, M., Obrizzo, F., Pingue, F., 2011. Multitemporal laser scanner-based observation of the Mt. Vesuvius crater: Characterization of overall geometry and recognition of landslide events. ISPRS Journal of Photogrammetry and Remote Sensing 66 (3), 327–336.

Pradhan, B., Jebur, M. N., Shafri, H. Z. M., Tehrany, M. S., 2015. Data fusion technique using Wavelet transform and Taguchi methods for automatic landslide detection from airborne laser scanning data and Quickbird satellite imagery. IEEE Transactions on Geoscience and Remote Sensing 54 (3), 1610–1622.

Rau, J.-Y., Jhan, J.-P., Rau, R.-J., 2014. Semiautomatic object-oriented landslide recognition scheme from multisensor optical imagery and DEM. IEEE Transactions on Geoscience and Remote Sensing 52 (2), 1336–1349.

Razak, K. A., Santangelo, M., van Westen, C. J., Straatsma, M. W., de Jong, S. M., 2013. Generating an optimal DTM from airborne laser scanning data for landslide mapping in a tropical forest environment. Geomorphology 190, 112–125.

Razak, K. A., Straatsma, M., van Westen, C., Malet, J.-P., De Jong, S., 2011. Airborne laser scanning of forested landslides characterization: terrain model quality and visualization. Geomorphology 126 (1), 186–200.

Rother, C., Kolmogorov, V., Blake, A., 2004. Grabcut: Interactive foreground extraction using iterated graph cuts. ACM Transactions on Graphics 23 (3), 309–314.

Saba, S. B., van der Meijde, M., van der Werff, H., 2010. Spatiotemporal landslide detection for the 2005 Kashmir earthquake region. Geomorphology 124 (1), 17–25.

Sato, H. P., Hasegawa, H., Fujiwara, S., Tobita, M., Koarai, M., Une, H., Iwahashi, J., 2007. Interpretation of landslide distribution triggered by the 2005 Northern Pakistan earthquake using SPOT 5 imagery. Landslides 4 (2), 113–122.

Scaioni, M., Longoni, L., Melillo, V., Papini, M., 2014. Remote sensing for landslide investigations: An overview of recent achievements and perspectives. Remote Sensing 6 (10), 9600–9652.

Sewell, R., Parry, S., Millis, S., Wang, N., Rieser, U., DeWitt, R., 2015. Dating of debris flow fan complexes from Lantau Island, Hong Kong, China: The potential relationship between landslide activity and climate change. Geomorphology 248, 205–227.

Szeliski, R., Zabih, R., Scharstein, D., Veksler, O., Kolmogorov, V., Agarwala, A., Tappen, M., Rother, C., 2008. A comparative study of energy minimization methods for markov random fields with smoothness-based priors. IEEE Transactions on Pattern Analysis and Machine Intelligence 30 (6), 1068–1080.

Tarolli, P., 2014. High-resolution topography for understanding Earth surface processes: opportunities and challenges. Geomorphology 216, 295–312.

Tarolli, P., Sofia, G., Dalla Fontana, G., 2012. Geomorphic features extraction from high-resolution topography: landslide crowns and bank erosion. Natural Hazards 61 (1), 65–83.

Tofani, V., Segoni, S., Agostini, A., Catani, F., Casagli, N., 2013. Technical Note: Use of remote sensing for landslide studies in Europe. Natural Hazards and Earth System Sciences 13 (2), 299–309.

Trevisani, S., Cavalli, M., Marchi, L., 2012. Surface texture analysis of a high-resolution DTM: Interpreting an alpine basin. Geomorphology 161, 26–39.

Tsutsui, K., Rokugawa, S., Nakagawa, H., Miyazaki, S., Cheng, C.-T., Shiraishi, T., Yang, S.-D., 2007. Detection and volume estimation of large-scale landslides based on elevation-change analysis using DEMs extracted from high-resolution satellite stereo imagery. IEEE Transactions on Geoscience and Remote Sensing 45 (6), 1681–1696.

van Den Eeckhaut, M., Kerle, N., Poesen, J., Hervás, J., 2012. Object-oriented identification of forested landslides with derivatives of single pulse LiDAR data. Geomorphology 173, 30–42.

van Westen, C., Getahun, F. L., 2003. Analyzing the evolution of the Tessina landslide using aerial photographs and digital elevation models. Geomorphology 54 (1), 77–89.

van Westen, C., van Asch, T. W., Soeters, R., 2006. Landslide hazard and risk zonation–why is it still so difficult? Bulletin of Engineering Geology and the Environment 65 (2), 167–184.

Ventura, G., Vilardo, G., Terranova, C., Sessa, E. B., 2011. Tracking and evolution of complex active landslides by multi-temporal airborne LiDAR data: the Montaguto landslide (Southern Italy). Remote Sensing of Environment 115 (12), 3237–3248.

Wood, J., Harrison, S., Reinhardt, L., 2015. Landslide inventories for climate impacts research in the European Alps. Geomorphology 228, 398–408.

Xu, C., Xu, X., Shyu, J. B. H., 2015. Database and spatial distribution of landslides triggered by the Lushan, China Mw 6.6 earthquake of 20 April 2013. Geomorphology 248, 77 – 92.

Xu, C., Xu, X., Yao, X., Dai, F., 2014. Three (nearly) complete inventories of landslides triggered by the May 12, 2008 Wenchuan Mw 7.9 earthquake of China and their spatial distribution statistical analysis. Landslides 11 (3), 441–461.

Yang, X., Chen, L., 2010. Using multi-temporal remote sensor imagery to detect earthquake-triggered landslides. International Journal of Applied Earth Observation and Geoinformation 12 (6), 487–495.

Yang, X., Lo, C., 2002. Using a time series of satellite imagery to detect land use and land cover changes in the Atlanta, Georgia metropolitan area. International Journal of Remote Sensing 23 (9), 1775–1798.

List of Figure Captions

Fig. 1. Study area with sub-areas A to D highlighted on Lantau Island, Hong Kong.

Fig. 2. Datasets. (a) and (b) Pre- and post-event aerial orthophotos. (c) Masked post-event orthophoto. (d) Reference map.

Fig. 3. Flowchart of the proposed landslide mapping method.

Fig. 4. Difference image (DI), the initial zero-level set (ZLS), and training sample masks. (a) DI generated by CVA. (b) The initial ZLS (white for landslides and black for non-landslides) generated by the single threshold method in Li et al., (2016) with $\alpha = 1.5$. (c) Training sample masks (red, green, and black

for landslides, non-landslides, and uncertain areas) generated by the multi-threshold method in Eq. (2) with $T = 1$ and $\Delta T = 1.5$. (d) - (g) Initial ZLSs in sub-areas A to D. (h) - (k) Training sample masks in sub-areas A to D.

Fig. 5. Diagram of MRF. Color_i is the ith Gaussian component G_i, $i = 1, ..., n$. n is fixed at 5 in this paper. Each GMM consists of 5 Gaussian components. GMM_1 and GMM_2 are the likelihood of landslide and non-landslide pixels, respectively. They are used to calculate the unary potential in Eq. (3). Gray and green nodes represent the landslide and non-landslide pixels, respectively. S and T correspond to the GMM_1 and GMM_2. The edge weights measure the degree of similarity of neighboring pixels (4-neighborhood system). They are employed to calculate the pairwise potential in Eq. (3). The larger the weights, the thicker the edges. The separations of the weak edges will automatically partition landslides from non-landslides.

Fig. 6. LM results of RLSE and the proposed CDMRF in the whole study area. (a) and (b) Results of RLSE and CDMRF overlaid on the post-event aerial orthophoto, respectively. (c) and (d) The corresponding binary results of RLSE and CDMRF.

Fig. 7. LM results in sub-area A. (a) and (b) Pre- and post-event aerial orthophotos. (c) reference map. (d)-(f) Results of RLSE: zero-level curve (ZLC) in (d), ZLS in (e), and the binary results in (f). (g)-(i) Result of CDMRF: landslide boundaries in (g), landslides in (h), and the binary results in (i). See main text for detailed explanations of the arrows in (d).

Fig. 8. LM results in sub-area B. (a) and (b) Pre- and post-event aerial orthophotos. (c) reference map. (d)-(f) Results of RLSE: ZLC in (d), ZLS in (e), and the binary results in (f). (g)-(i) Result of CDMRF: landslide boundaries in (g), landslides in (h), and the binary results in (i). See main text for detailed explanation of the arrow in (d).

Fig. 9. LM results in sub-area C. (a) and (b) Pre- and post-event aerial orthophotos. (c) reference map. (d)-(f) Results of RLSE: ZLC in (d), ZLS in (e), and the binary results in (f). (g)-(i) Result of CDMRF: landslide boundaries in (g), landslides in (h), and the binary results in (i). See main text for detailed explanations of the arrows in (d).

Fig. 10. LM results in sub-area D. (a) and (b) Pre- and post-event aerial orthophotos. (c) reference map. (d)-(f) Results of RLSE: ZLC in (d), ZLS in (e), and the binary results in (f). (g)-(i) Result of CDMRF: landslide boundaries in (g), landslides in (h), and the binary results in (i). See main text for detailed explanations of the arrows in (d).

Fig. 11. Quantitative evaluation of the proposed CDMRF for LM in the whole study area and four sub-areas A to D. (a). Completeness. (b) Correctness. (c) Quality.